

Hyperbolic phonon-polaritons in boron nitride for near-field optical imaging

Peining Li¹, Martin Lewin^{1,2}, Andrey V. Kretinin,³ Joshua D. Caldwell^{4*}, Kostya S. Novoselov,³ Takashi Taniguchi,⁵ Kenji Watanabe,⁵ Fabian Gaussmann², Thomas Taubner^{1,2*}

1 Institute of Physics (IA), RWTH Aachen University, Aachen 52056, Germany

2 Fraunhofer Institute for Laser Technology ILT, 52074 Aachen, Germany

3 School of Physics and Astronomy, University of Manchester, Oxford Rd, Manchester, UK

4 U.S. Naval Research Laboratory, 4555 Overlook Ave, S.W., Washington, D.C. USA

5 National Institute for Materials Science, 1-1 Namiki, Tsukuba, Ibaraki 305-0044, Japan

*Correspondence to: joshua.caldwell@nrl.navy.mil and taubner@physik.rwth-aachen.de

Optical imaging beyond the diffraction limit was one of the primary motivations for negative-index metamaterials, resulting in Pendry's perfect lens and the more attainable superlens. While these approaches offer sub-diffractive resolution, they do not provide a mechanism for magnification of the image. Hyperbolic (or indefinite-permittivity) metamaterials have been theoretically considered and experimentally demonstrated to provide simultaneously subdiffractive imaging and magnification; however, they are plagued with low efficiency and complex fabrication. In this work, we present theoretical and experimental studies of near-field optical imaging through a flat slab of the low-loss,

natural hyperbolic material, hexagonal boron nitride (hBN). This thin hBN layer exhibits wavelength-dependent multifunctional operations, offering both an enhanced near-field imaging of single buried objects with down to $\lambda/32$ resolution (0.4 μm at $\lambda=12.8 \mu\text{m}$), as well as enabling an enlarged reconstruction of the geometric outline of the investigated objects. Both the excellent resolution and the multifunctional operation can be explained based on the volume-confined, wavelength dependent propagation angle of Type I hyperbolic polaritons. Our results provide both the understanding of near-field imaging performance through this natural hyperbolic media, as well as inspire their exciting potential for guiding and sensing of light at an extreme sub-diffractive scale.

Introduction

The propagation of sub-diffractive waves in hyperbolic media¹ enables many unusual optical applications such as hyperlensing^{2,3,4}, negative refraction^{5,6}, enhanced quantum radiation⁷, nanolithography⁸ and sub-diffractive resonators^{9,10}. Very recently, it was demonstrated that the highly directional propagation of volume-confined, hyperbolic polaritons (HPs) is key for these sub-diffractive phenomena^{8,10,11}. Their directionality derives from the sign and magnitude of the two principal (in- and out-of-plane) components of the dielectric-permittivity tensor ($\vec{\varepsilon} = \text{diag}[\varepsilon_{xx}, \varepsilon_{yy}, \varepsilon_{zz}]$), which have opposite signs. The propagation angle θ (e.g. the angle between the Poynting vector and the z-axis) of the HPs in hyperbolic media can be roughly approximated as¹⁰,

$$\theta = \pi/2 - \arctan(\sqrt{\varepsilon_z(\omega)}/i\sqrt{\varepsilon_t(\omega)}) \quad (1)$$

where $\epsilon_t = \epsilon_{xx} = \epsilon_{yy}$ and $\epsilon_z = \epsilon_{zz}$ are the in- and out-of-plane dielectric permittivities of the hyperbolic medium, respectively. Therefore, by controlling the ratio of the two principal dielectric components, the propagation direction of the HPs can be tuned.

Until very recently, hyperbolic media have been explored through man-made hyperbolic metamaterial structures, such as metal-dielectric multilayers^{4,5}, nanowire^{6,12} or nano-pyramid arrays⁹ embedded within a dielectric medium. In hyperbolic metamaterials (HMMs), the effective dielectric permittivities are determined by the geometric parameters of their subwavelength unit cells¹. As such, the maximum wavevector \mathbf{k} that can be induced to propagate through the material is limited by the size of the artificial unit cell. This in turn limits the degree of optical confinement and spatial resolution that can be realized. Furthermore, the high losses associated with noble metals used in man-made hyperbolic metamaterial structures^{13,14,15} result in short propagation lengths, quite broad resonance linewidths and in terms of hyperlens designs, low transmission efficiency.

During the search for better “plasmonic” materials^{14,15}, polar dielectrics capable of supporting phonon-polaritons such as silicon carbide^{16,17,18,19,20} and hBN^{10,11,21} have been demonstrated as superior alternatives to metals at mid-infrared and THz frequencies. Interestingly, many phonon-resonant materials such as quartz²², zinc oxide²³, calcite²⁴ and hBN^{10,11,21} are also natural hyperbolic materials²⁵ (NHMs). These NHMs support HPs within homogeneous crystals with atomic-scale unit cells, thus the upper limit on the highest propagating wavevectors \mathbf{k} associated with artificial metal-dielectric HMMs is no longer an issue. Instead, photonic confinement within tiny volumes in the few nanometer range becomes possible. This was recently demonstrated by Dai *et al.*¹¹ where surface phonon polariton propagation within a 3 monolayer (<1 nm) thin flake of hBN was reported. It is the propagation of such high- \mathbf{k} fields that are scattered off or launched

from deeply sub-diffractive objects that is at the heart of super-resolution imaging. These benefits are also coupled with a drastic reduction in the optical losses compared to HMMs, which results in improved performance, i.e. higher field confinement^{10,11} and improved image resolution.

In contrast to HMMs reported to date, hBN offers the additional functionality of sub-wavelength imaging at different spectral regions through the presence of two separate spectral bands exhibiting hyperbolic response. These two regimes are referred to as the lower and upper Reststrahlen bands^{10,11}, where this term refers to the spectral range between the longitudinal (LO) and transverse (TO) optic phonons of a polar crystal where a negative real part of the dielectric function is observed. The presence of these two bands results from the highly anisotropic crystal structure of hBN, where both a,b- and c-axis oriented optical phonons are supported and are widely separated in frequency²⁶. As displayed in Fig. 1, these two bands not only exhibit hyperbolic behavior, but the crystal axis featuring negative real permittivity can be inverted, thus the lower and upper bands offer Type-I ($\text{Re}(\varepsilon_t) > 0$ and $\text{Re}(\varepsilon_z) < 0$ in $760 < \omega < 825 \text{ cm}^{-1}$) and Type-II ($\text{Re}(\varepsilon_t) < 0$ and $\text{Re}(\varepsilon_z) > 0$ in $1360 < \omega < 1610 \text{ cm}^{-1}$) hyperbolic response, respectively. In addition, the imaginary part of the hBN is quite small, i.e., $\text{Im}(\varepsilon_t) \sim 0.1$ for $\text{Re}(\varepsilon_t) = -1$ at $\omega = 809 \text{ cm}^{-1}$ and $\text{Im}(\varepsilon_z) \sim 0.1$ for $\text{Re}(\varepsilon_z) = -1$ at $\omega = 809 \text{ cm}^{-1}$, which is very crucial for the extended propagation and detection of high- \mathbf{k} polariton mode^{10,11,17}.

The dielectric permittivities are also highly dispersive in these two regions, giving rise to a frequency-dependent ratio between ε_t and ε_z . Thus, from Eq. (1) we know that the propagation angle θ will be an increasing (decreasing) function of the frequency in the lower (upper) Reststrahlen bands. As shown in Fig. 2 a and b, as the frequency is increased, θ increases from about 16° to 87° ($\Delta\theta \approx 71^\circ$) within the Type I lower Reststrahlen band while it decreases from θ

$\approx 83^\circ$ to $\theta \approx 2^\circ$ ($\Delta\theta \approx 81^\circ$) in the Type II upper Reststrahlen band. This inversion in the frequency dispersion in the HP propagation angle is directly related with the previously reported inverted shift in the frequencies of higher order HPs within hBN nanoresonators reported by Caldwell *et al.*¹⁰.

Results and discussions

This frequency-dependent tuning of the angular HP propagation in hBN and the suitability of this material for near-field imaging can be easily quantified and visualized via two-dimensional (2D) numerical calculations. For this, we consider a 0.3 μm wide gold stripe on a Si substrate with an hBN cover layer (the thickness $h = 1 \mu\text{m}$) illuminated by a p -polarized plane wave incident from the top. Simulated electric-field distributions ($|\mathbf{E}_z|$) at six typical operation frequencies are presented in Figs. 2c-h, and demonstrate the directional nature of the HPs. Here the high- \mathbf{k} fields scattered from the edges of the embedded gold stripe are induced to propagate within the hBN flake (as marked in Fig. 2d), with the angle of propagation being directly dependent upon the frequency of operation. As stated previously¹⁻⁴, in the absence of the hyperbolic dispersion, such high- \mathbf{k} modes would be evanescent (i.e. decay rapidly) within the medium. Each edge of the Au stripe excites two sub-diffractive HPs that propagate at the angles $\pm \theta$. This frequency dependent propagation angle quantitatively agrees with the analytical predictions based on Eq. (1) (see Fig. 2a and b), therefore the propagation angle can be predicted via the simple ratio of the extraordinary and ordinary components of the anisotropic dielectric function of hBN.

The anticipated super-resolution imaging performance of the hBN slab is directly tied to the propagation angle, as demonstrated in Figs. 2c-h. For instance, at wavelengths with very low propagation angles (Figs. 2 c and f), the image of the sub-diffractive Au stripe is nearly perfectly

restored on the top surface of the hBN, similar to near-field superlensing^{27,28,29}. Namely, the restored width d' is nearly identical to the actual width d of the investigated stripe (e.g. $d' \approx 309$ nm, around $\lambda/40$ -resolution at $\omega = 778.2 \text{ cm}^{-1}$ or $\lambda = 12.85 \text{ }\mu\text{m}$). However, as the angle is increased (Figs, 2d,e for the lower and g,h for the upper Reststrahlen bands), an enlarged outline of the object image is obtained with the width $D(\omega) = d + 2 h \tan\theta(\omega)$.

This novel enlargement can be clearly seen in the more practical three-dimensional (3D) cases. As shown in Fig. 2i, the 0.6- μm -diameter gold disc is once again perfectly restored at very shallow angles; however, at larger propagation angles a double concentric ring-like field distribution is recorded in the near-field (Fig. 2j), rather than a direct replication of the original field distribution of the object. This enlarged pattern results from the frequency-dependent propagation angle of the HPs (cone-like shape for 3D case, see the sketch in Fig. 2k). Namely, the trace of the HP cones form the enlarged and slightly distorted pattern (compared to the actual object fields, due to the polarized illumination) that is still able to identify the outline information of the object (see more simulation results in Supplementary Information). Therefore, by changing the illumination wavelength, the imaging functionality of the hBN slab can be tuned from a near-perfect imaging with a one-to-one reconstruction of the object to a tunable enlargement ($\sim D(\omega)/d$) for near-field imaging of single objects.

The predicted imaging mechanism is verified by our experiments, as presented in Fig. 3. A schematic of the experimental setup is provided in Fig. 3a where the images restored by the hBN layer are recorded using a scattering-type scanning near-field optical microscope (s-SNOM). We use a 0.15- μm -thick exfoliated hBN flake to image the underlying, 30 nm tall, gold nanodiscs with 0.3- μm diameter and 1.3- μm center-to-center separation. The metallic tip of the s-SNOM is illuminated by a homebuilt, tunable broadband infrared laser^{30,31} with the peak position of the

laser spectrum (insert in Fig. 3a) matched to the lower, Type-I hyperbolic region of hBN ($760 \text{ cm}^{-1} < \omega < 825 \text{ cm}^{-1}$). Both the optical and topographic information at the top surface of the hBN layer are collected simultaneously (details in Methods). We note that the response in the upper Type-II hyperbolic region of hBN is studied independently by another group using commercial quantum-cascade lasers (QCLs)³². In the obtained topographic image (Fig. 3b), the gold discs are masked by the covering hBN layer, while in the broadband-SNOM image (Fig. 3c), all three nanodiscs are clearly resolved with bright contrast (i.e. high signal-to-background ratio). To ensure that the imaging is indeed due to the hyperbolic nature of the hBN slab, a control image was also collected at a frequency outside of the lower Reststrahlen band using a CO₂ laser at $\omega = 952 \text{ cm}^{-1}$, where both components of the dielectric function are positive ($\text{Re}(\epsilon_t) = 8.8$ and $\text{Re}(\epsilon_z) = 2$). As shown in Fig. 3e, in contrast to the hyperbolic case, only weak features of the discs are observed through the thin hBN layer in the control experiment. This is further demonstrated by the line profiles taken across the two discs for both cases presented in Fig. 3f, with a dramatic enhancement in the imaging efficiency observed in the hyperbolic regime. The hyperbolic images also provided a narrower FWHM (full width at half maximum) of about $0.5 \mu\text{m}$ in addition to the dramatically improved contrast (signal-to-background ratio). Considering the resolved deeply subwavelength optical FWHM ($\sim \lambda/24$), this comparison clearly confirms the improved near-field imaging by the hBN layer.

Although the broadband s-SNOM image shown in Fig. 3c is able to resolve the discs, it does not reflect the actual field distribution of the image due to its detection scheme³¹. Because of the broadband light source used, the detection is not monochromatic as in the simulations presented in Fig. 2. Instead, the collected images are the superposition of all the different frequency components of the broadband laser and therefore the concentric-ring field distributions are not

directly observed. Further, depending on the chosen interference phase difference (constructive or destructive phases, involving the position of a reference mirror in our setup, see Methods), it can also show reversed imaging contrasts³¹. Therefore, the broadband s-SNOM image alone cannot directly reveal the actual image field distributions of the discs and the frequency dependence of the hBN layer. For this, monochromatic s-SNOM images would be required; however, currently such sources are not readily available within this spectral range.

To determine the actual imaging response through the hBN layer at each individual wavelength, we performed Fourier transform infrared nanospectroscopy (nano-FTIR)^{11,31} along a line scan (dashed line in Fig. 3c) across two discs. At each pixel, nano-FTIR delivers a full IR spectrum recorded at the spatial resolution of the probing tip (~ 50 nm). Thus we obtain s-SNOM signals $s_2(\omega, x)$ as a function of the frequency ω and the spatial position x .^{11,16,29} This hyperspectral imaging allows the extraction of detailed spatial line profiles at various frequencies as shown in Fig. 3g. For frequencies $\omega > 780$ cm^{-1} , two peaks are observed for each disc (see the typical case at $\omega = 783$ cm^{-1}). These peaks (with the width $d' \sim 0.3$ μm , Supplementary Information) correspond to the edge-excited HPs. The distance D between the two edge-launched peaks increases from about 0.4 μm to approximately 1.25 μm (for the right disc) when changing the frequency from 780 cm^{-1} to 807 cm^{-1} . At frequencies $\omega < 780$ cm^{-1} , the two edge-launched peaks are not resolved by the hBN layer, leading to one single broad peak observed for each disc. Based on the smallest peak-to-peak separation in our results being approximately 0.4 μm at $\omega = 780$ cm^{-1} ($\lambda = 12.8$ μm), this corresponds to a sub-diffractive resolution of about $\lambda/32$ (also see Supplementary Information).

For the comparison of the theoretically predicted propagation angles (Fig. 2a) and those experimentally derived from the s-SNOM measurements, we plot the experimentally determined

D (blue curve and data) and corresponding directional angles θ (red curve and data) of the HPs as functions of ω in Fig. 3h. The theoretical result [from $D(\omega) = d + 2h \tan\theta(\omega)$] is also shown for comparison. Good quantitative agreement is found between the experiments and theory. This verifies the predicted tuning range of the propagation angle of the HPs to be about 35° – 70° and the tunable ratio (D/d) to range from 1.39 to 4.2. However, certain discrepancies are still found in this comparison, and we do not observe multiple peaks originating from the multi-reflection of the HPs within the hBN slab. Our work and ref. 32 demonstrate the complete hyperbolic imaging response of hBN and its potential for improving the near-field imaging of deeply embedded objects^{33,34} in both the Type I lower and Type II upper Reststrahlen bands, respectively. More specifically, we reveal the hyperbolic nature of the hBN layer for near-field imaging and its dependence upon the operational frequency. Although all our results are restricted in the near field, we also expect that these novel findings will benefit far-field imaging by introducing specific geometric designs, such as circular or wedge-shaped hyperlenses^{2,3}.

Summary and outlook

In addition to the already proven high-resolution imaging with tunable enlargement of the outline of sub-diffractive objects, we can also envision other potential disruptive technologies based on the great potential of the highly directional HPs. The strongly dispersive angle of propagation could be exploited for sub-diffractive wavelength multiplexing into multiple nanoscale waveguides. Figure 4a shows numerical simulations of HPs propagating inside an hBN waveguide structure (a horizontal hBN-layer connected with three vertical hBN-channels) at a frequency of $\omega = 762 \text{ cm}^{-1}$. Due to the small propagation angle, the electromagnetic fields primarily propagate into the inner ‘0’-channel. When tuning the frequency to $\omega = 778.2 \text{ cm}^{-1}$ (Fig. 4b), the fields propagate with an angle of $\sim 45^\circ$ and therefore transmit into the two outer ‘1’-

channels. More complicated geometries could also expand such approaches beyond a binary routing into more sophisticated multi-channel systems. Consequently, this frequency-selective waveguiding could be useful for photonic switching or computing, infrared filtering, or various other nanophotonic applications. Another potential application is realized in the form of an ultra-compact subwavelength spectrometer. As sketched in Fig. 4c, a natural hBN layer should allow for the spatial separation or filtering of incoming broadband light into different wavelength channels, which could then be detected by subwavelength IR detector pixels. This particular spectrometer configuration could also be used for chemical and biological samples, in the form of spatially-resolved infrared spectroscopy. Under broadband mid-infrared illumination the HPs could carry the vibration (or absorption) information of molecules in contact with the surface (Fig. 4d), dispersing the spectral information at different angles, enabling them to be spatially resolved by a near-field intensity detector (like the s-SNOM tip) without the need of spectrometers.

All these examples of the new variety of nanophotonic applications can be realized via the use of HPs in hBN that go even beyond sub-diffractive near-field imaging and potential hyperlensing. Due to the similar material anisotropy present in other polar dielectric van der Waals crystals³⁵, such as MoS₂ or WS₂, the natural hyperbolic response of hBN may also be expected to be general to the entire class of polar two-dimensional crystals, thus expanding the potential spectral range of this behavior from the mid-IR into the single digit THz spectral region^{17,24}.

Methods Summary

Sample preparation. The gold nanostructures used for the near-field experiments were fabricated on a 1- μm -thick intrinsic silicon substrate using electron beam lithography into a bilayer PMMA resist. The nanostructures varied in size from 0.2-1 μm in diameter and in arrays with 0.1-1 μm edge-to-edge gaps. A standard liftoff procedure was used following the thermal evaporation of Cr (5 nm)/Au (30 nm) metallization.

Hexagonal BN crystals were grown using the high-pressure/high-temperature method^{36,37}. The standard exfoliation process was used to randomly deposit hBN flakes of various thicknesses onto a PMMA/PMGI bilayer spun on a separate silicon substrate. Here the PMMA layer played the role of the flake carrier membrane and the PMGI served as a sacrificial lift-off layer later dissolved by TMAH solution (MICROPOSIT[®] MF[®]-319). Atomic force microscopy was utilized to select specific flakes with both sufficient thickness and lateral size for the imaging experiments. The PMMA carrier membrane with an appropriate hBN flake was lifted-off from the substrate and put onto the supportive metal ring held by a home-made micromanipulator. With the help of the micromanipulator, the hBN flake was aligned and transferred face down onto the predefined gold nanostructure by releasing the carrier membrane from the metal ring. Following the transfer, the sample with the carrier membrane on was heated to 130°C for about 10 min to soften the PMMA membrane and improve the adhesion of hBN to the underlying nanostructures and silicon substrate. After that the carrier membrane was dissolved in acetone leaving the hBN flake covering the entire array of nanostructures. To improve the adhesion, an ultrasonic clean in acetone and isopropyl alcohol with subsequent oxygen plasma clean was performed on the silicon substrate prior to the hBN transfer. More details of this transfer technique are given in Ref. 38.

Infrared broadband s-SNOM measurements. An s-SNOM (commercially available, Neaspec GmbH) system with a broadband module was used to simultaneously measure the optical near fields and topography. The laser system used for our SNOM measurements was developed by the Fraunhofer ILT^{30,31}. It consists of a commercially available ps-laser as the pump source and two subsequent nonlinear converter steps to cover the mid-IR range. The peak wavelength is continuously tunable from $\omega = 625 \text{ cm}^{-1}$ ($\sim 16 \mu\text{m}$) to $\omega = 1100 \text{ cm}^{-1}$ ($\sim 9 \mu\text{m}$) with bandwidths of some tens to more than hundred wavenumbers. At a repetition rate of 20 MHz and pulse duration of 10 ps, the system provides an average power of up to 10 mW. To address the lower Type-I hyperbolic region of the hBN, the peak position of the laser spectrum in our measurements was set to be at around $\omega = 790 \text{ cm}^{-1}$ ($12.7 \mu\text{m}$) with a FWHM of about 90 cm^{-1} . To suppress the far-field background contribution and solely measure the near-field contribution, the optical signal s was demodulated at higher harmonics of the oscillation frequency Ω of the cantilever (2Ω in our case, s_2). Nano-FTIR spectra were obtained by constantly moving the mirror in the reference arm of the Michelson interferometer, recording the resulting interferograms and their corresponding complex Fourier transformation^{11,31}. In contrast to conventional far-field FTIR, this setup allows to record spectral information with a spatial resolution of down to several tens nm. For 2D imaging, the position of the reference mirror was fixed to be at the position about $\lambda/8$ away from the maximum of the interference signals. This allows for a visualization of even small spectral changes³¹. The extracted line profiles shown in Fig. 3g were numerically smoothed by using a fast Fourier Transform (FFT) smoothing with 3 adjacent pixels. This smoothing does not improve the resolution, but rather leads to a conservative estimation of resolution (details in Supplementary Information).

Numerical simulations. 2D simulations (Figs. 2c-d) were carried out by the finite-element software COMSOL Multiphysics. A plane-wave illumination was set by using scattering boundary condition. The surrounding boundaries used perfectly matched layer absorbing boundary conditions. 3D simulations (Figs. 2i-k) were done by using CST Microwave Studio™. Open boundary conditions were used. We also checked different mesh sizes to make sure that all the simulations reach proper convergence. The dielectric data of hBN shown in Fig. 1b and used in all the simulations are extracted from far-field FTIR measurements¹⁰.

Acknowledgments

This work was supported by the Excellence Initiative of the German federal and state governments, the Ministry of Innovation of North Rhine-Westphalia, the DFG under SFB 917 and the Korean Defense Acquisition Program Administration and the Agency for Defense Development as a part of a basic research program under the contract UD110099GD. Funding for JDC was provided by the NRL Nanoscience Institute and was carried out at the University of Manchester through the NRL Long-Term Training (Sabbatical) Program. A.K. and K.S.N. acknowledge support from the Engineering and Physical Sciences Research Council (UK), The Royal Society (UK), European Research Council and EC-FET European Graphene Flagship.

References

1. Poddubny, A., Iorsh, I., Belov, P. & Kivshar, Y. Hyperbolic metamaterials. *Nature Photon.* **7**, 948–957 (2013).
2. Jacob, Z., Alekseyev, L. V. & Narimanov, E. Optical hyperlens: far-field imaging beyond the diffraction limit. *Opt. Express* **14**, 8247–8256 (2006).

3. Salandrino, A. & Engheta, N. Far-field subdiffraction optical microscopy using metamaterial crystals: theory and simulations. *Phys. Rev. B* **74**, 075103 (2006).
4. Liu, Z., Lee, H., Xiong, Y., Sun, C. & Zhang, X. Far-field optical hyperlens magnifying sub-diffraction-limited objects. *Science* **315**, 1686 (2007).
5. Hoffman, A. J. *et al.* Negative refraction in semiconductor metamaterials. *Nature Mater.* **6**, 946–950 (2007).
6. Yao, J. *et al.* Optical negative refraction in bulk metamaterials of nanowires. *Science* **321**, 930(2008).
7. Krishnamoorthy, H. N. S., Jacob, Z., Narimanov, E., Kretzschmar, I. & Menon, V. M. Topological transitions in metamaterials. *Science* **336**, 205–209 (2012).
8. Ishii, S., Kildishev, A. V., Narimanov, E., Shalaev, V. M. & Drachev, V. P. Sub-wavelength interference pattern from volume plasmon polaritons in a hyperbolic medium. *Las. Photon. Rev.* **7**, 265–271 (2013).
9. Yang, X., Yao, J., Rho, J., Yin, X. & Zhang, X. Experimental realization of three-dimensional indefinite cavities at the nanoscale with anomalous scaling laws. *Nature Photon.* **6**, 450–454(2012).
10. Caldwell, J. D. *et al.*, Sub-diffraction, volume-confined polaritons in the natural hyperbolic material: hexagonal boron nitride. *Nat. Comms.* **5**, 5221 (2014).
11. Dai S. *et al.* Tunable phonon polaritons in atomically thin van der Waals crystals of boron nitride. *Science* **343**, 1125 (2014).

12. Prokes, S.M. *et al.* Hyperbolic and Plasmonic Properties of Silicon/Ag aligned Nanowire Arrays, *Opt. Express* **21**, 14962 (2013).
13. Khurgin J. B & Boltasseva A. Reflecting upon the losses in plasmonics and metamaterials. *MRS Bull.* **37**, 768-779 (2012).
14. West, P. R., Ishii, S., Naik, G. V., Emani, N. K., Shalae, V. M., & Boltasseva, A. Searching for better plasmonic materials. *Las. Photon. Rev.* **4**, 795 (2010).
15. Tassin, P., Koschny, T., Kafesaki, M., & Soukoulis, C. M. A comparison of graphene, superconductors and metals as conductors for metamaterials and plasmonics. *Nature Photon.* **6**, 259-264 (2012).
16. R. Hillenbrand, T. Taubner, & F. Keilmann, Phonon-enhanced light–matter interaction at the nanometre scale. *Nature* **418**, 159 (2002).
17. Caldwell, J. D., Lindsay, L., Giannini, V., Vurgaftman, I., Reinecke, T. L., Maier, S. A., & Glembocki, O. J. Low-loss, infrared and terahertz nanophotonics using surface phonon polaritons. *Nanophotonics*, <http://dx.doi.org/10.1515/nanoph-2014-0003> (2014).
18. Caldwell, J. D. et al. Low-loss, extreme sub-diffraction photon confinement via silicon carbide surface phonon polariton nanopillar resonators. *Nano Lett.* **13**, 3690-3697, (2013).
19. Wang T., Li P., Hauer B., Chigrin D. N. & Taubner T. Optical properties of single infrared resonant circular microcavities for surface phonon polaritons. *Nano Lett.* **13**, 5051 (2013).
20. Chen Y., Francescato Y., Caldwell J.D., Giannini V., Mass T., Bezares F. J., Taubner T., Kasica R., Hong M., Maier S. A. Tracking the role of proximity and size for localized surface phonon polariton resonators, *ACS Photonics*, **1**, 718-724 (2014).

21. Xu X. G. *et al.* One-dimensional surface phonon polaritons in boron nitride nanotubes. *Nat. Comms.* **5**, 4782(2014).
22. Da Silva R. E., Macedo R., Dumelow T., Da Costa J. A. P., Honorato S. B. & A. P. Ayala. Far-infrared slab lensing and subwavelength imaging in crystal quartz. *Phy. Rev. B* **86**, 155152 (2012).
23. Fonoberov V. A. & Balandin A. A. Polar optical phonons in wurtzite spheroidal quantum dots: theory and application to ZnO and ZnO/MgZnO nanostructures. *J. Phys.: Condens. Matter* **17**, 1085 (2005).
24. Thompson, D. W., De Vries, M. J., Tiwald, T. E., & Woollam, J. A. Determination of optical anisotropy in calcite from ultraviolet to mid-infrared by generalized ellipsometry. *Thin Solid Films*, **313**, 341-346 (1998).
25. Sun, J., Litchinitser, N. M., Zhou, J., Indefinite by nature: from ultraviolet to terahertz. *ACS Photonics* **1**, 293 (2014).
26. Geick, R., Perry, C. H., & Rupprecht, G. Normal modes in hexagonal boron nitride. *Phy. Rev. B*, **146**, 543 (1966).
27. J. B. Pendry, Negative refraction makes a perfect Lens. *Phys. Rev. Lett.* **85**, 3966 (2000).
28. Fang N. *et al.* Sub-diffraction-limited optical imaging with a silver superlens. *Science* **308**, 534 (2005).
29. Taubner T., Korobkin D., Urzhumov Y., Shvets G. & Hillenbrand R. Near-field microscopy through a SiC superlens. *Science* **313**, 159 (2006).

30. Wueppen, J., Jungbluth, B., Taubner, T., & Loosen, P. Ultrafast tunable mid IR source. In *Infrared, Millimeter and Terahertz Waves (IRMMW-THz)*, 36th-International Conference, IEEE, pp. 1-2 (2011).
31. Bensmann, S. *et al.* Near-field imaging and spectroscopy of locally strained GaN using an IR broadband laser. *Opt. Express* **22**, 22369-22381 (2014).
32. Dai S. *et al.* Subdiffractional focusing and guiding of polaritonic rays in a natural hyperbolic material. Submitted (2014).
33. Taubner T., Keilmann F., Hillenbrand R. Nanoscale-resolved subsurface imaging by scattering-type near-field optical microscopy. *Opt. Express* **13**, 8893-8899 (2005).
34. Li, P., Wang, T., Böckmann, H., & Taubner, T. Graphene-enhanced infrared near-field microscopy. *Nano Lett.* **14**, 4400-4405 (2014).
35. Geim, A. K. & Grigorieva, I. V. Van der Waals heterostructures. *Nature* **499**, 419-425, (2013).
36. Taniguchi, T. & Watanabe, K. Synthesis of high-purity boron nitride single crystals under high pressure by using Ba-BN solvent. *J. Cryst. Growth* **303**, 525-529, (2007).
37. Watanabe, K., Taniguchi, T. & Kanda, H. Direct-bandgap properties and evidence for ultraviolet lasing of hexagonal boron nitride single crystal. *Nature Materials* **3**, 404-409, (2004).
38. A. V. Kretinin *et. al*, Electronic Properties of Graphene Encapsulated with Different Two-Dimensional Atomic Crystals. *Nano Lett.* **14**, 3270-3276, (2014).

Figure Legends

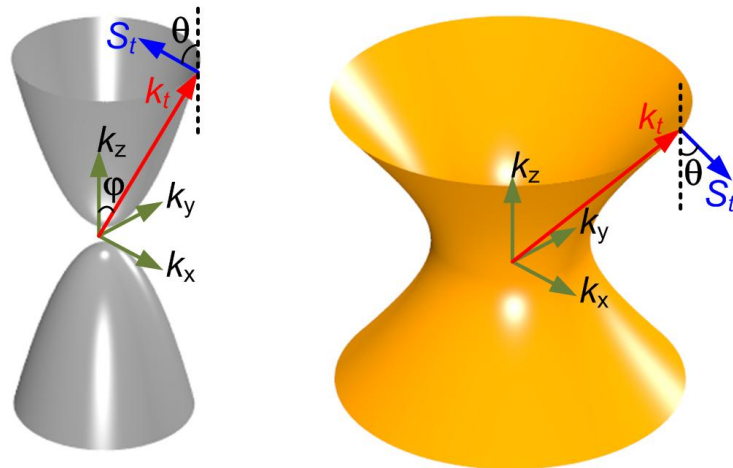
Figure 1. Hyperbolic dispersion in a hBN layer. Top, two types of hyperbolic dispersions (the Type I for $\text{Re}(\varepsilon_t) < 0$ and $\text{Re}(\varepsilon_z) > 0$ and the Type II for $\text{Re}(\varepsilon_t) > 0$ and $\text{Re}(\varepsilon_z) < 0$) and their corresponding vector diagrams. φ is the angle between the wavevector \mathbf{k}_t and z axis. θ is the angle between the Poynting vector \mathbf{S}_t and z axis. For large wavevectors ($k_x \gg k_0$, $k_0 = 2\pi/\lambda$), $\varphi + \theta \approx \pi/2$. Bottom, in-plane and out-plane dielectric permittivities (ε_t , ε_z) of hBN, taken from the ref.10. Two hyperbolic regions are marked in gray and yellow, respectively.

Figure 2. Frequency-dependent directional angles of the HPs propagating inside the hBN. Solid lines in **a** and **b**, the critical angle θ of the HPs as a function of the frequency ω in the Type-I ($760 < \omega < 825 \text{ cm}^{-1}$, $\varepsilon_t < 0$ and $\varepsilon_z > 0$) and Type-II ($1360 < \omega < 1610 \text{ cm}^{-1}$, $\varepsilon_t > 0$ and $\varepsilon_z < 0$) hyperbolic bands of the hBN. **c-h**, Simulated electric-field distribution ($|E_z|$) at various frequencies. The directional angles evaluated from these simulations are plotted in **a** and **b** (color dots) for comparison: $\theta = 16^\circ$ (**c**, at $\omega = 761 \text{ cm}^{-1}$), $\theta = 2^\circ$ (**f**, at $\omega = 1613.8 \text{ cm}^{-1}$), $\theta = 45^\circ$ (**d** and **g**, at $\omega = 778.2 \text{ cm}^{-1}$ and $\omega = 1527 \text{ cm}^{-1}$) and $\theta = 60^\circ$ (**e** and **h**, at $\omega = 795 \text{ cm}^{-1}$ and $\omega = 1459.6 \text{ cm}^{-1}$). The scale bar in **c** indicates $1 \mu\text{m}$. **i** and **j**, 3D simulations of imaging a gold disc ($0.6\text{-}\mu\text{m}$ diameter) below the $1\text{-}\mu\text{m}$ -thick hBN layer (scale bar 300 nm , z -axis not to scale for better visualization). Simulated electric-field distributions ($|E_z|$) taken at top and bottom surface of the hBN layer for imaging, **i**, at $\omega = 761 \text{ cm}^{-1}$. **j**, at $\omega = 778.2 \text{ cm}^{-1}$ show the frequency-dependent transition between perfect imaging and enlarged imaging. **k**, the sketch of the mechanism of the enlargement observed in **j**. (In this sketch we do not consider the influence of the illumination polarization)

Figure 3. Experimental demonstration of super-resolution imaging with tunable HPs in the hBN hyperlens. **a**, Sketch of the experimental set-up. The right inset is the normalized laser spectrum of the used mid-infrared broadband laser. **b**, The AFM topography taken at the top surface of the 0.15- μm -thick hBN hyperlens. **c**, The 2D infrared optical images taken with the broadband laser. **e**, The control infrared image taken with a CO_2 laser at $\omega = 952 \text{ cm}^{-1}$ that is out of the hyperbolic region of the hBN. The small black dots in the image are caused from topographic features (corresponding topographic image shown in **d**). Scale bars: 0.5 μm . **f**, Detailed profiles of the s-SNOM signals across two neighboring discs (along the line marked in **e**, averaged over 5 scan lines) for the cases using the broadband laser (red line) and the CO_2 laser (black line), respectively. Both profiles are normalized to their respective minimum values outside the discs. The broadband imaging shows much stronger contrasts for the discs. **g**, Detailed Nano-FTIR line profiles at various frequencies. Dashed line marks the position variations of the peak of edge-launched HPs. **h**, Optical widths and corresponding directional angles of the HPs evaluated from the experimental results (dots) in comparison with the calculated results (solid lines). The error bars result from the spatial pixel ($\sim 50 \text{ nm}$) in nano-FTIR measurements.

Figure 4. Further application proposals using the tunable highly directional HPs. Simulated $|E_z|$ -distributions inside an hBN waveguiding structure **a** at $\omega = 761 \text{ cm}^{-1}$, **b** at $\omega = 778.2 \text{ cm}^{-1}$. **c**, Sketches of an ultra-compact hBN-based infrared spectrometer. The thin hBN layer allows spatially splitting different wavelength components of the incoming infrared illumination. **d**,

Sketches of hBN-based spatially-resolved infrared spectroscopy for different molecules. The dark colors in the spectrum represent the absorption by the molecules (sketch).



Type I: $\text{Re}(\epsilon_t) > 0$, $\text{Re}(\epsilon_z) < 0$ Type II: $\text{Re}(\epsilon_t) < 0$, $\text{Re}(\epsilon_z) > 0$

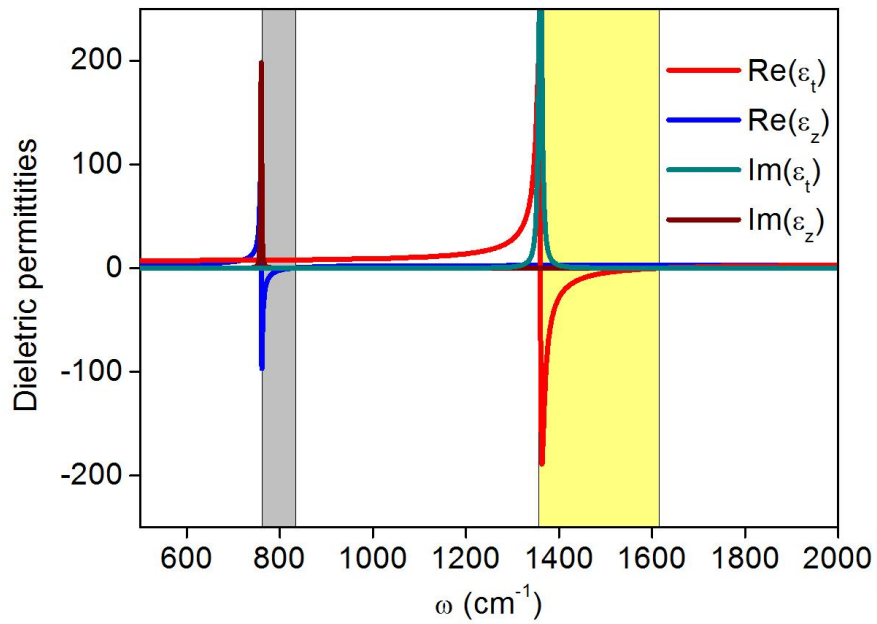


Figure 1

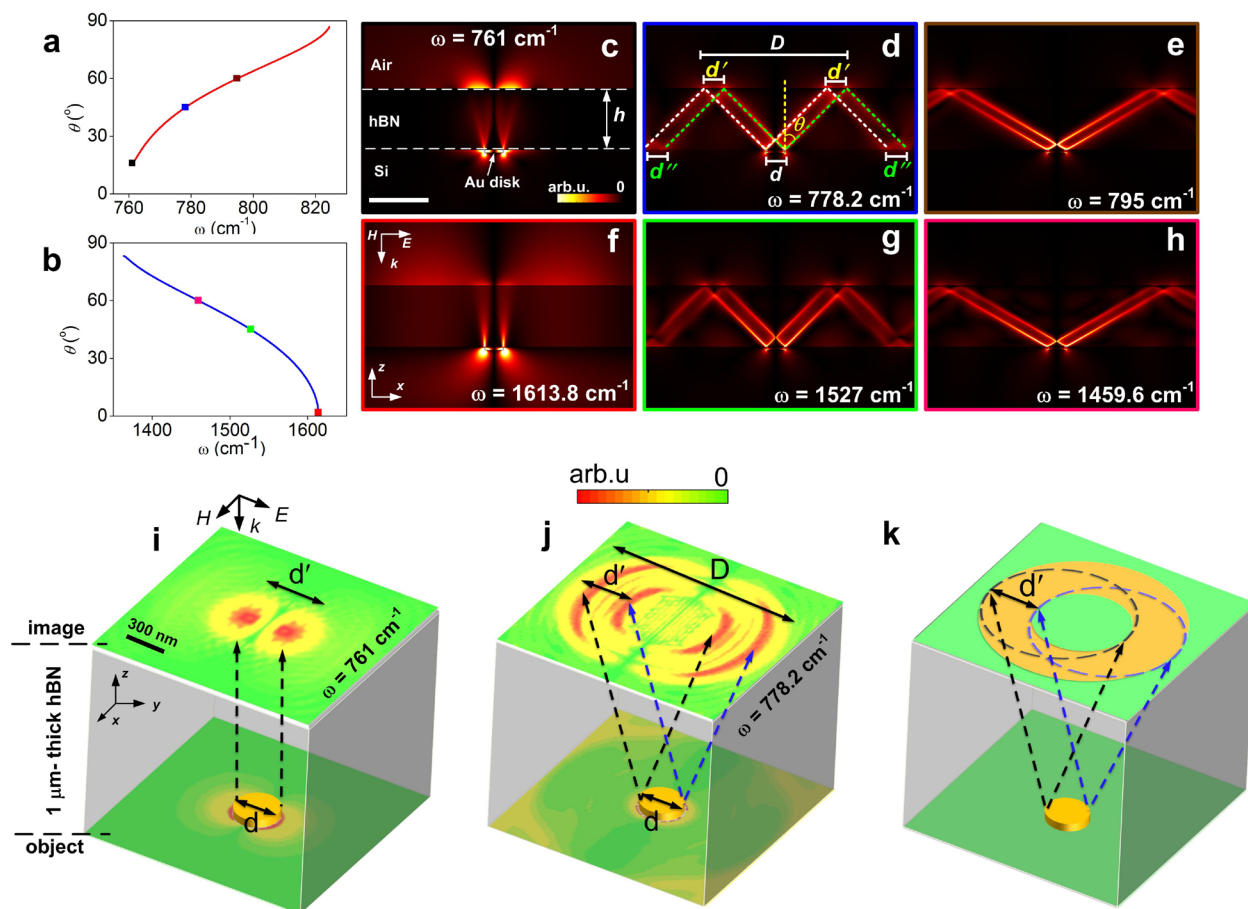


Figure 2

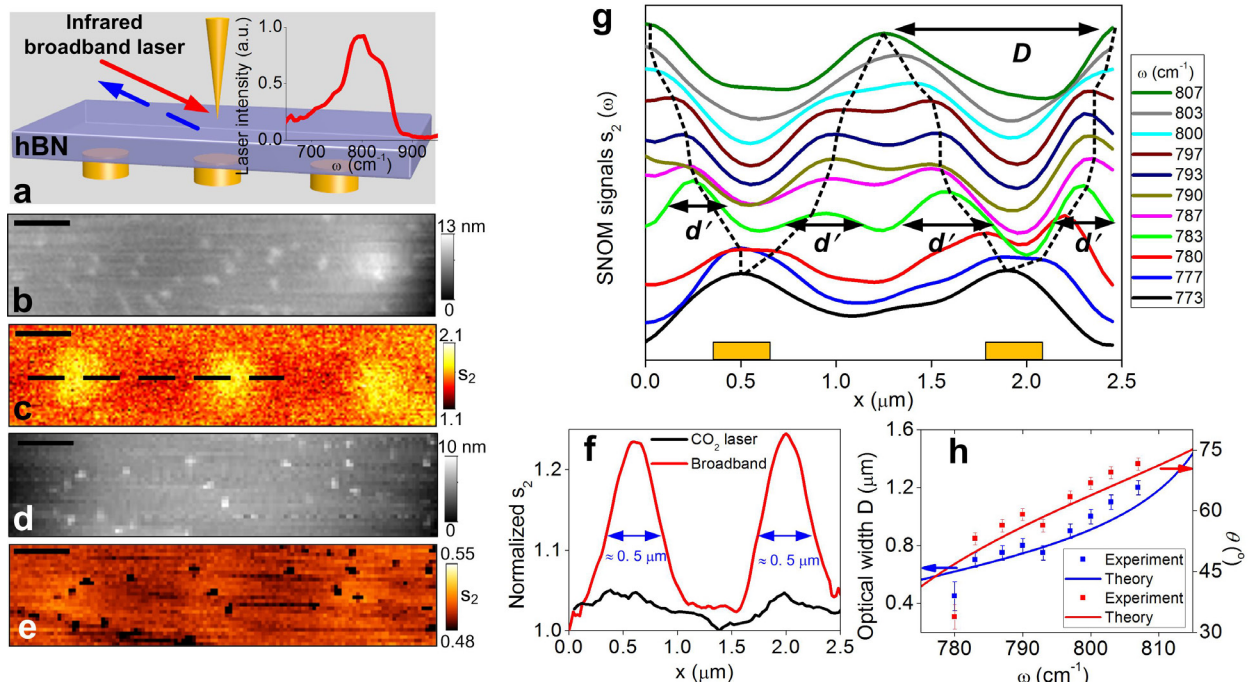


Figure 3

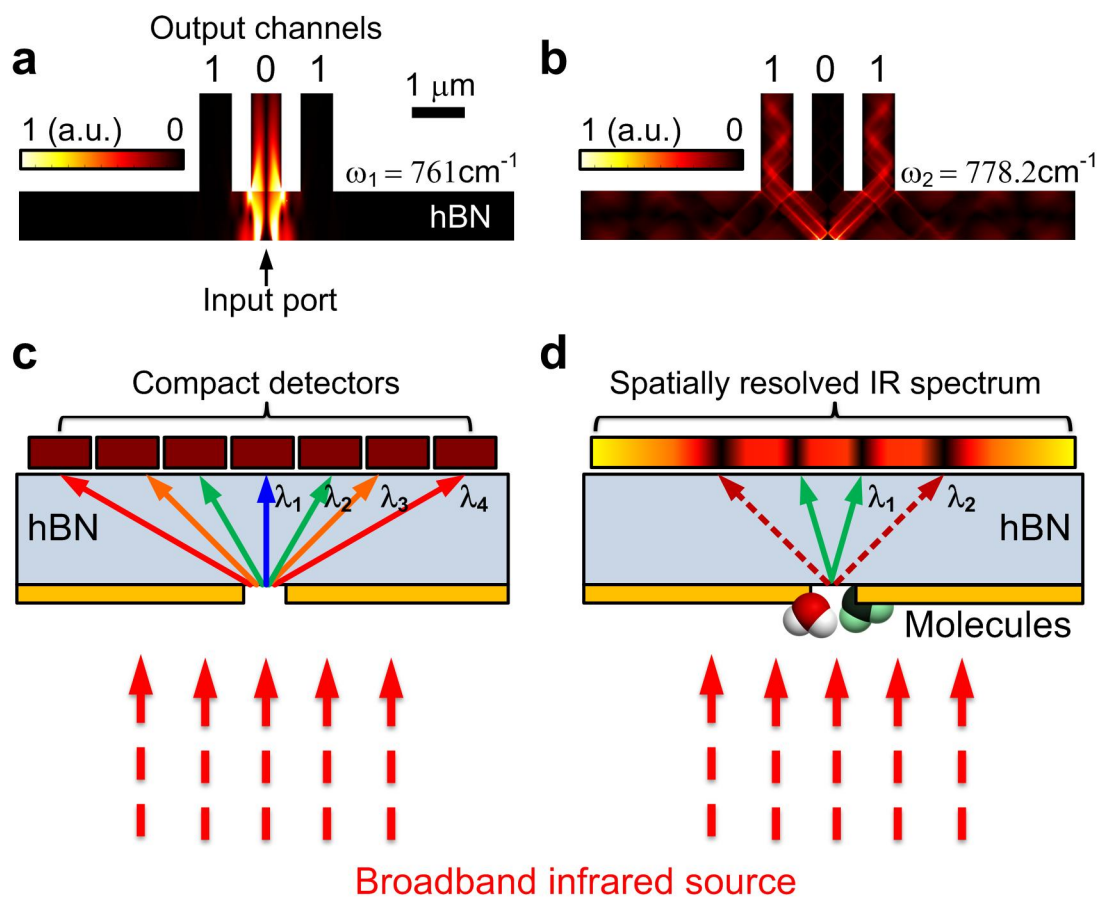


Figure 4